Molecular dynamics simulation of the adsorption of organic contaminants (phthalate esters and perfluorinated alkyl substances) on organic-coated smectite clay particles

Jennifer A. R. Willemsen[1,*], Meléa Emunah[1], Ian C. Bourg[1]

[1]Department of Civil & Environmental Engineering (CEE) and High Meadows Environmental Institute (HMEI), Princeton University, Princeton, NJ 08544, USA

*email: jwillemsen1825@gmail.com

Abbreviations:

DFT, density functional theory

DEP, diethyl phthalate

DMP, dimethyl phthalate

HDTMAB, hexadecyltrimethylammonium bromide

MD, molecular dynamics

NERSC, National Energy Research Scientific Computing Center

PFAS, per- and polyfluoroalkyl substances

PFBS, perfluorobutanesulfonic acid

PFOA, perfluorooctanoic acid

PFOS, perfluorooctanesulfonic acid

PPPM, particle-particle/particle-mesh

SOM, soil organic matter

TNB, Temple-Northeastern-Birmingham

Abstract:

Molecular dynamics (MD) simulations are used to examine the adsorption and aggregation of tyrosine and glutamate molecules on a stack of smectite particles at three different organic loadings. The results reveal a strong affinity of the smectite surface for the organic molecules, with the zwitterionic tyrosine molecules coating the exterior surfaces (and entering the interlayer region to a lesser extent) while the negatively charged glutamate molecules are generally found near the clay edge sites and in coordination with aqueous and coordinating calcium ions. Additional simulations examine the effects of the tyrosine and glutamate organic coatings on the adsorption of two organic contaminants, dimethyl phthalate (DMP) and perfluorobutanesulfonic acid (PFBS). The addition of these coatings did not prevent the DMP and PFBS molecules from accessing previously identified favorable adsorption domains. An analysis of the adsorption energetics shows an initial decrease in contaminant adsorption relative to pure mineral surfaces as tyrosine and glutamate are introduced to the system, followed by increasing adsorption with increasing organic loadings. Overall, this research advances the mechanistic understanding of the interplay between smectite surfaces, organic coatings, and organic contaminants.

1. Introduction

In the natural environment, organic carbon is found in soils at levels more than quadruple that of atmospheric CO_2, with important implications for the Earth's carbon cycle, soil fertility, and soil resilience to erosion and drought (Ciais et al., 2013; Friedlingstein et al., 2019; Lehmann & Kleber, 2015). This organic carbon is found predominantly within soil organic matter (SOM), a complex mixture of organic substances characterized in part by its tendency to associate with mineral surfaces (Kleber et al., 2015; Kleber et al., 2021; Mayer, 1993; Ranson et al., 1997). In temperate regions, observations suggest a particularly close association between SOM and high surface area phyllosilicate minerals, such as smectite clay (Ransom et al., 1997; Rasmussen et al., 2018). These SOM-mineral interactions have important implications for the dynamics of soil carbon and organic contaminants. In particular, they are widely believed to alter the microbial processing of SOM (and associated carbon emissions) (Kleber et al., 2021; Lehmann & Kleber, 2015; Mayer, 1993; Ransom et al., 1997; Sulman et al., 2014) and the adsorptive capacity of mineral surfaces for anthropogenic organic contaminants (and hence the fate and transport of these contaminants) (Celis et al., 1998; Jeon et al., 2011; Li et al., 2003; Tian et al., 2016; Wu et al., 2015; Zhou et al., 2010).

For both phenomena outlined above, fundamental understanding of the impact of SOM-mineral interactions remains limited, in large part because of the complex and variable nature of SOM (Hsu et al., 2018; Lehmann & Kleber, 2015; Marín-Spiotta et al., 2014; Ohno et al., 2017). Whereas the adsorption of individual organic compounds on soil minerals is increasingly well understood (Newcomb et al., 2017) knowledge of the manner in which SOM coats mineral

surfaces (and of the impact of these coatings on the adsorption of other compounds) remains limited (Coward et al., 2019; Kleber et al., 2021; Lee et al., 2008). In fact, even the fundamental mechanisms by which silicate minerals bind SOM molecules and aggregates remain incompletely understood: anion exchange, cation bridging, hydrophobic interactions, Van der Waals forces, and hydrogen bonding have all been variously proposed to be of key importance (Kleber et al., 2021; Lützow et al., 2006; Zhang, et al., 2020).

In the last decade, atomistic simulations—including particularly molecular dynamics (MD) and density functional theory (DFT) simulations—have emerged as a useful tool in the study of mineral-organic interactions. In examinations of the adsorption of individual organic molecules, these simulations have demonstrated strong complementarity with nanoscale experimental approaches (Aristilde et al., 2016; Kwon et al., 2006; Liu et al., 2019; Schampera et al., 2016). In studies of SOM, they may prove particularly valuable (Greathouse et al., 2014) as the complexity of SOM binding mechanisms and supra-molecule structures strongly limits the feasibility of deconvolving experimental data (Kleber et al., 2021). Although significant challenges exist with regard to the examination of SOM and SOM-mineral interactions using atomistic simulations, notably with regard to the definition of SOM proxies and the generation of equilibrium structures for SOM aggregates on the limited time-scale of these simulations, previous MED simulation studies have successfully examined the aggregation of various more or less simple or realistic SOM proxies (ranging from single molecules to mixtures of ~10 compounds) under different aqueous chemistry conditions (Devarajan et al., 2020; Iskrenova-Tchoukova et al., 2010; Kalinichev, 2012; Loganathan et al., 2020) along with the behavior of

these proxies in mesopores (Loganathan et al., 2020), interlayer regions (Kelch et al., 2019; Sutton & Sposito, 2006), and on edge surfaces of smectite clay particles (Zhang et al., 2020).

In this paper, we build upon previous studies to examine the influence of an organic matter coating on the adsorption of organic contaminants on smectite clay. We focus on two contaminants—dimethyl phthalate (DMP), an uncharged polar chemical plasticizer, and perfluorobutanesulfonic acid (PFBS), a short chained anionic surfactant in the family of per- and polyfluoroalkyl substances (PFAS)—for which we previously characterized adsorption on pristine smectite using MD simulations. Previous atomistic simulation studies of the adsorption of similar contaminants on organic-coated minerals have modeled PFAS adsorption on organic-coated silica surfaces and within an organic-coated Na-smectite nanopore, but these studies simulated very short time scales (2.1 ns or less) and did not quantify the free energy of adsorption of the organic contaminant (Yan et al., 2020; Zhang et al., 2015). Previous experimental studies have observed significantly enhanced adsorption of perfluorooctanesulfonic acid (PFOS) and perfluorooctanoic acid (PFOA) on smectite clay in the presence of cationic surfactants such as hexadecyltrimethylammonium bromide (HDTMAB) (Tian et al., 2016; Zhou et al., 2010), while humic acid, tannic acid, and Suwannee River natural organic matter coatings resulted in decreased PFOS and PFOA adsorption compared to pure smectite surfaces (Jeon et al., 2011). Wu et al. (2015) found that diethyl phthalate (DEP) adsorption on K-smectite was ten times greater when the surfaces were coated with humic acid at organic carbon loadings ranging from 0.0015 to 0.015 g_{carbon}/g_{clay}. These results, along with experimental data for organic contaminant adsorption by SOM-coated smectite more broadly (Celis et al., 1998; Li et al., 2004), are somewhat contradictory as they show that SOM coatings can either increase or

decrease contaminant adsorption depending on contaminant type, clay counterion type, and the nature of the examined SOM (or SOM proxy).

In an attempt to shed light on the impact of organic matter coatings on the adsorption of organic contaminants, we first examine the coatings formed by a mixture of amino acids (as a simplified model of mineral-associated SOM, see next section) on montmorillonite surfaces. Specifically, simulations are conducted at three organic loadings reflecting low (0.01 g_{carbon}/g_{clay}), medium (0.05 g_{carbon}/g_{clay}), and high ranges (0.1 g_{carbon}/g_{clay}) of the organic carbon to clay mass ratios observed in soils and sediments (Mayer, 1993). Then, we apply a metadynamics-based MD simulation methodology developed in our previous studies (Willemsen & Bourg, 2021; Willemsen et al., 2019) to predict the impact of these coatings on the free energies of adsorption of DMP and PFBS. Adsorption mechanisms and energetics are analyzed and compared to our previous results on DMP and PFBS adsorption on pristine smectite surfaces (Willemsen & Bourg, 2021; Willemsen et al., 2019). Overall, this work has the potential to improve understanding of mineral-organic matter interactions and the fate and transport of organic contaminants and also has implications for the development of organo-clay adsorbents (Tian et al., 2016; Yan et al., 2020; Zhou et al., 2010; Zhou et al., 2015).

2. Methods

2.1 Simplified Model of Mineral-Associated SOM

As noted above, a recurrent challenge in understanding mineral-organic interactions in soils and sediments is the complex and variable structure of SOM. The emerging view suggests that SOM

131 is comprised of organic fragments varying in size and at various stages of decomposition
132 (Lehmann & Kleber, 2015; Sutton & Sposito, 2005). These fragments can range from large plant
133 and animal residues to small biopolymers and monomers. Previous MD simulation studies have
134 represented this complex material using a variety of simple SOM proxies (Greathouse et al.,
135 2014) including the macromolecular Schulten model (Sutton & Sposito, 2006), the Vienna model
136 (Escalona et al., 2021; Petrov et al., 2017; Zhang et al., 2020), the Temple-Northeastern-
137 Birmingham (TNB) model (Iskrenova-Tchoukova et al., 2010; Kalinichev, 2012; Loganathan et
138 al., 2020), the UT/ORNL model of dissolved organic matter (Devarajan et al., 2020), fatty acids
139 (Aquino et al., 2011), and a hydrophobic nanopore comprised of aliphatic chains and carboxyl
140 groups (Tunega et al., 2019). A compilation of SOM proxies used in previous MD simulation
141 studies is presented in Table 1. The proxies presented in Table 1 obviously greatly simplify the
142 complexity of SOM, yet they have proved useful in generating fundamental insight into the
143 processes that underlie key behaviors of SOM. In this work, we focus on necromass, the dead
144 microbial component of SOM that accounts for anywhere from 30% (in the case of temperate
145 forest soils) to 61.8% (in the case of grassland soils) of total topsoil organic carbon (Liang et al.,
146 2019). Compared to larger plant-based SOM components, necromass tends to contain more polar
147 and ionizable groups and is more readily found in association with mineral surfaces (Buckeridge
148 et al., 2020; Liang et al., 2017; Liang et al., 2019; Totsche et al., 2018), making it of particular
149 interest for our study. As a highly simplified model of soil microbial necromass, we choose a 1:1
150 combination of glutamate, an anionic amino acid at neutral pH, and tyrosine, a zwitterionic
151 amino acid. Although this proxy obviously underestimates the complexity of microbial
152 necromass, its complexity is similar to that of many of the proxies used in previous MD
153 simulations (Table 1). Its combined C:H:O:N elemental ratio (14:19:7:2) is consistent with

154 commonly used models of microbial biomass stoichiometry (5:7:2:1) (Christensen & McCarty,
155 1975) and with reported biomass C:N ratios (5 to 8) (Kleber et al., 2017; Xu et al., 2013) and is
156 reasonably close to C:N ratios reported for the fine-sized fraction of soils (on the order of 10 to
157 12) (Totsche et al., 2018). Finally, we note that individual amino acids have been used as simple
158 proxies for mineral-associated organic matter in at least one previous experimental study (Gao et
159 al., 2017).
160
161 Table 1: Molecular formulas and structural descriptions of SOM proxies used in previous
162 molecular dynamics simulation studies.

SOM Proxy	Molecular Formula	Structure	Reference
Schulten Model (humic acid)	$C_{447}H_{421}O_{272}N_{15}S_2$	Macromolecule	Sutton & Sposito, 2006
Vienna Model	Varies	Associations of small organic molecules (system specific)	Escalona et al., 2021; Petrov et al., 2017; Zhang et al., 2020
TNB Model	$C_{36}H_{37}O_{16}N_2$	One molecule	Iskrenova-Tchoukova et al., 2010; Kalinichev, 2012; Loganathan et al., 2020
UT/ORNL Model	$C_{679}H_{965}O_{282}N_{38}S_6P$ $C_{577}H_{849}O_{326}N_{23}S_3P$	Combination of light weight organic compounds and peptide, carbohydrate, and lignin components	Devarajan et al., 2020
Undecanoid acid	$CH_3(CH_2)_9COOH$	4 molecules oriented such that carboxylate groups form a hydrophilic center	Aquino et al., 2011
Hydrophobic nanopore	$C_{37}H_{72}$	One 15C and two 11C aliphatic chains	Tunega et al., 2019

		connected to form a hydrophobic nanopore	
Glutamate and tyrosine amino acids	$C_5H_8O_4N$ (glutamate) $C_9H_{11}O_3N$ (tyrosine)	5, 26, or 52 of each molecule added and allowed to aggregate	This study

2.2 Molecular Dynamics Simulations

Molecular dynamics simulations were performed using methodologies adapted from our previous studies (Willemsen & Bourg 2021; Willemsen et al., 2019) to examine DMP and PFBS adsorption by organic-coated mineral surfaces at three different organic loadings, for a total of six unique conditions. Each simulated system consisted of a periodically replicated simulation cell containing 9960 water molecules and a stack of two fully flexible Ca-montmorillonite particles (60 unit cells) with an interlayer spacing of 6 Å and randomly distributed octahedral Al^{3+} to Mg^{2+} isomorphic substitutions in accordance with Löwenstein's avoidance rule. The resulting structural charge densities were -0.60 and -0.55 e per unit cell for the upper and lower clay lamellae, respectively. Three DMP or PFBS molecules were added to the system with a background electrolyte solution of 0.18 M or 0.10 M $CaCl_2$, respectively, to match the concentrations used in our prior studies of adsorption on pristine smectite surfaces (Willemsen & Bourg, 2021; Willemsen et al., 2019). Five glutamate and five tyrosine molecules were added to the simulation cell for the system with a low organic loading, 26 each in the medium loading system, and 52 each in the high loading system. Calcium ions were added as necessary to charge-balance the negatively charged glutamate molecules and to maintain charge-neutrality in the system.

Simulations were carried out on the Cori supercomputer at the National Energy Research Scientific Computing Center (NERSC) using the LAMMPS program (Plimpton, 1995) and the Colvars package (Fiorin et al., 2013). Glutamate, tyrosine, DMP, and PFBS were parameterized using the OPLS-AA force field (Jorgensen et al., 1996; Lopes & Pádua, 2004). Interatomic interactions for the clay particles and cleaved edge surfaces were described using the CLAYFF model (Cygan et al., 2004) with the extended CLAYFF parameterization of Lammers et al. (2017). Water molecules were simulated using the SPC/E model (Berendsen et al., 1987), and calcium and chloride ions using well-established models (Åqvist, 1990; Smith & Dang, 1994). Details can be found in Table S1 in the Supplementary Information. The use of distinct force fields developed to simulate mineral-water (CLAYFF) and organic-water systems (OPLS-AA) requires particular care as the compatibility of these models has not been rigorously tested. Furthermore, these models use slightly different conventions for various details of the interatomic interactions. Notably, they use different mixing rules to evaluate Lennard-Jones 6-12 pair potential parameters between non-identical atom types. To account for this difference, parameters for interactions between organic molecules were calculated using the convention of the OPLS-AA force field, $\epsilon_{ij} = \sqrt{\epsilon_{ii}\epsilon_{jj}}$ and $\sigma_{ij} = \sqrt{\sigma_{ii}\sigma_{jj}}$, where ϵ_{ij} and σ_{ij} are the interatomic potential well depth and the distance at which the potential equals zero and *i* and *j* are different atom types (Jorgensen et al., 1996). All other Lennard-Jones potential parameters between non-identical atom types were calculated using the convention of the CLAYFF force field, whereby $\sigma_{ij} = \frac{1}{2}\left(\sigma_{ii} + \sigma_{jj}\right)$ (Cygan et al., 2004). We also note that the interatomic potential models used in this study, like most standard models used in classical MD simulations, were not designed to represent changes in covalent bonding. Therefore, our simulations inherently cannot predict the covalent adsorption of organic molecules on clay edge surfaces or the associated ligand-

206 promoted dissolution of clay edges.

207

208 Glutamate and tyrosine molecules were initially placed in the bulk water region of the simulation
209 cell and all simulations were first equilibrated for 445 ps, including a 200 ps run in the NPT
210 ensemble (P_y = 1 bar) to allow the volume of the box to equilibrate. The resulting simulation cell
211 size was 63.36 Å × 89.19 Å × 65.0 Å, with variations by up to 2.58 Å in the *y* dimension with
212 changing organic loadings. An additional 60 ns equilibration run was then conducted in the NVT
213 ensemble at 298 K to allow the glutamate and tyrosine molecules to explore the simulation cell
214 and coat the clay surface (Figure 1). Contaminant molecules were frozen in place, far from the
215 clay surface, over the course of both equilibration runs in order to first allow the glutamate and
216 tyrosine molecules to interact with the clay particles. Following equilibration, the DMP and
217 PFBS molecules were allowed to move freely. The SHAKE algorithm (Ryckaert et al., 1997)
218 was used to keep water molecules rigid, and the clay layers were constrained by setting their
219 translational and rotational velocities to zero with the exception of translation in the *z* direction,
220 thus allowing for changes in the interparticle distance. The clay layers were otherwise fully
221 flexible. Short range VdW and Coulomb interactions were solved up to 12 Å, and long range
222 Coulomb interactions beyond the cutoff were calculated using the particle-particle/particle-mesh
223 (PPPM) Ewald summation method (Eastwood et al., 1980) with 99.9% accuracy.

224

225 ## 2.3. Metadynamics Simulations

226 Metadynamics simulations were run in the NVT ensemble at 298 K for up to 515 ns. Two
227 collective variables, the *y* and *z* coordinates of the contaminant molecule's center of mass, were
228 used to evaluate the free energy landscape associated with the location of the contaminant in the

simulation cell. Metadynamics was performed independently on each of the three contaminant molecules in each simulation, thus allowing for statistical error calculations. Simulations were concluded once the free energy landscapes of the three replicates converged with similar free energy differences between the bulk water and clay regions. Metadynamics simulation specific information about the duration and size of Gaussian bias potential deposition can be found in Table S2 of the Supplemental Information. Free energies of adsorption were calculated for the entire stack of clay lamellae as well as in different sub-regions (i.e., within 6 Å of the upper and lower external basal surfaces and in the interlayer region) by temporally and spatially averaging two-dimensional free energy maps over the last 50 ns of the metadynamics simulations as described in the Supplemental Information and in our previous papers (Willemsen & Bourg 2021; Willemsen et al., 2019). In addition to the metadynamics simulations, standard "unbiased" simulations were performed for 75 to 100 ns to characterize favorable contaminant binding structures on the basal surface.

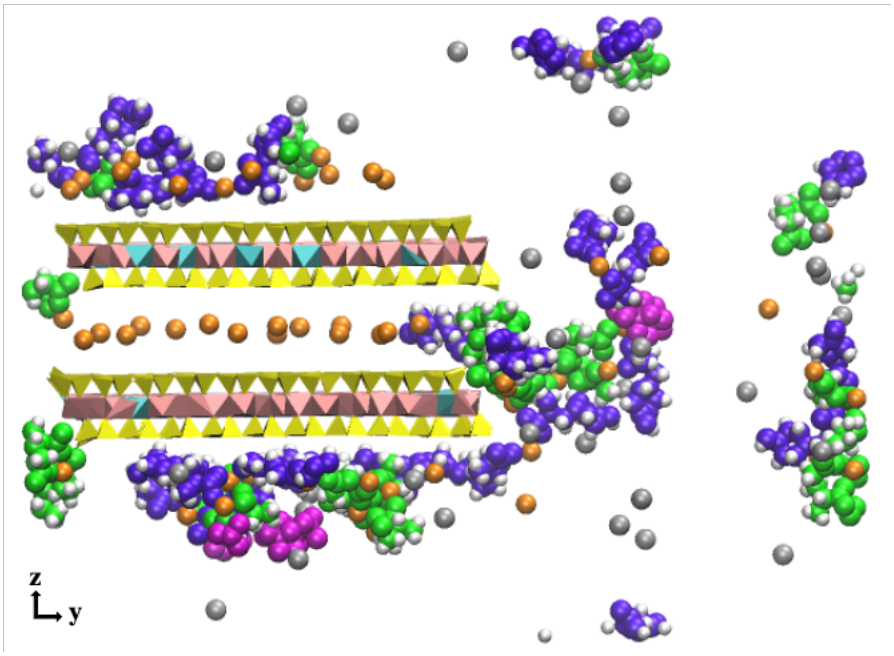

Figure 1: Snapshot of the system with a low organic loading (0.05 g_{carbon}/g_{clay}) showing PFBS, glutamate, and tyrosine molecules as pink, green, and purple spheres (with their H atoms as white spheres). Calcium and chloride ions are shown as orange and grey spheres. Water molecules are rendered invisible for viewing purposes. The organic molecules on the right side of the image interact with the left surface of the stack of clay particles through the periodic boundary of the simulation cell.

3 Structure of the Organic Coating

3.1 Organic Coating Distribution on the Stack of Clay Particles

Output from the unbiased simulations was analyzed to create two-dimensional density maps for glutamate, tyrosine, and calcium at low, medium, and high organic loadings. Results are shown in Figure 2 for systems containing DMP and Figure S1 for systems containing PFBS. Similar behavior was observed in both sets of simulations. The results reveal the existence of density maxima near the clay surfaces, indicating that the simulated amino acids have a strong affinity for these surfaces. Essentially complete adsorption is observed at low and medium organic loadings, i.e., no glutamate or tyrosine density is observed in the bulk liquid water region, defined as the 63.36 Å × 10 Å × 65 Å region of the simulation box at the greatest distance from the clay edges (on the right side of the simulation cell). At the highest loading, organic density in the bulk liquid water region is nonzero, suggesting a saturation of available adsorption domains even though the clay surface is not fully coated by organic matter. Free organic aggregates (i.e., aggregates of several organic molecules not attached to the clay surface) are observed in this bulk liquid water region.

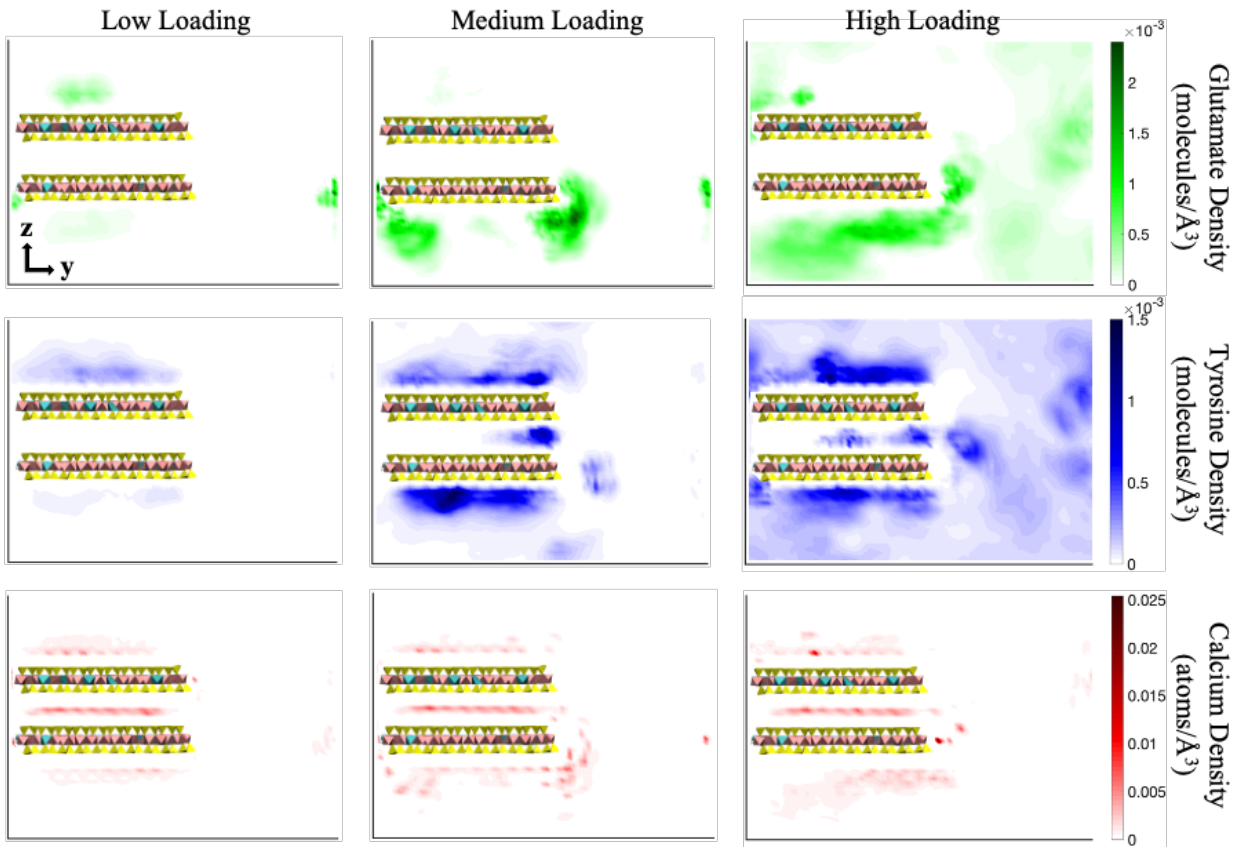

Figure 2: Average glutamate (green), tyrosine (blue), and calcium (red) density in the *yz* plane for the simulations containing DMP at different organic loadings. Results were averaged over the last 70 ns of the unbiased simulations.

Tyrosine density peaks are observed adjacent to the exterior basal surfaces, indicative of inner-sphere complex formation with the clay surface. At the high organic loading, a second layer of tyrosine density is observed adjacent to the first adsorbed monolayer of tyrosine molecules, indicating the formation of a multilayer coating. Some tyrosine intercalation is also observed at medium and high loadings, possibly enabled by the slight planar character of this molecule, though organic density in the interlayer region remains lower than on the external basal surfaces.

The glutamate molecules exhibit a propensity to form aggregates with calcium ions near the surface, as evidenced by increased calcium density in regions with high glutamate density and in agreement with previous studies of SOM aggregation and adsorption (Iskrenova-Tchoukova et al., 2010; Kalinichev, 2012; Loganathan et al., 2020; Sowers et al., 2018). No glutamate is found in the interlayer region as expected given its size and anionic nature. The greater accumulation of organic matter on exterior surfaces rather than the interlayer nanopores is consistent with previous studies (Loganathan et al., 2020). The preferential adsorption of tyrosine vs. glutamate on the basal surface is consistent with experimental results indicating a stronger adsorption of zwitterionic vs. anionic amino acids to smectite clay (Yeasmin et al., 2014).

3.2 Aggregation Structure in the Organic Coating

Detailed examination of the simulation trajectories confirms both the formation of a multi-layer coating (with a "contact layer" of tyrosine coated by aggregates of glutamate) and the strong association between adsorbed organic molecules and Ca ions. These findings are consistent with the so-called "onion-skin" conceptual model of SOM surface coatings and with the role of Ca-bridging interactions suggested in previous studies (Coward et al., 2019; Kleber et al., 2007; Sowers et al., 2018). However, simulation snapshots also reveal that the organic coating is discontinuous even at high loadings where the presence of organic molecules in bulk solution suggests a saturation of surface sites, in agreement with experimental observations (Chenu & Plante, 2006; Totsche et al., 2018). A potential clue into the origin of this patchy coverage is provided by observations that at the highest organic loading, portions of the basal surface that are not coated by organic matter are consistently devoid of adsorbed Ca ions (as illustrated in Figure

3). This suggests that the lateral extent of the organic coating on the clay basal surface may be limited by the abundance of Ca counterions present on this surface, which should be sensitive to clay surface charge density.

Detailed examination of the predicted structure of the organic coating further shows that glutamate molecules also exhibit a strong affinity for clay edge surfaces. In our simulations, these surfaces carry no net charge, in accordance with current estimates of their protonation state near pH 7 (Tournassat, Davis, et al., 2016). However, they do carry localized regions of positive charge (Tournassat, Bourg, et al., 2016) that may allow for favorable electrostatic interactions with negatively charged glutamate molecules.

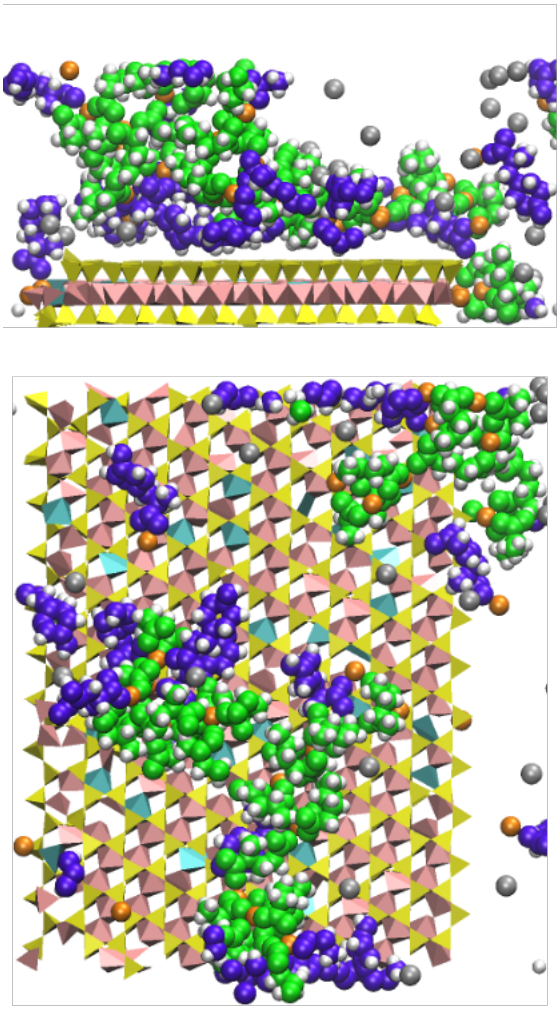

Figure 3: Snapshots of the system with a high organic loading containing DMP molecules viewed along the *yz* (top) and *xy* (bottom) planes highlighting the structure of the organic coating on one of the external basal surfaces. The color scheme is the same as in Figure 1.

3.3 Hydrophilic/Hydrophobic Nature of the Clay Surface

Our previous MD simulation studies of organic contaminant partitioning to a stack of smectite sheets revealed that adsorption of uncharged phthalate esters and anionic perfluoroalkyl substances (PFAs) was enhanced on the less charged clay sheet (0.55 versus 0.60 structural charges per unit cell) with the greatest contaminant density concentrated on patches of the clay

siloxane surface spatially distant from the isomorphic substitutions (Willemsen & Bourg, 2021; Willemsen et al., 2019). Here, we examine whether glutamate and tyrosine molecules also preferentially adsorb to these uncharged regions. For this, average atomic densities within 7 Å of the plane of the lower basal surface oxygens were calculated over the last 70 ns of the unbiased simulations and compared with the location of isomorphic substitution sites in the underlying clay particle. This 7 Å region was chosen to fully capture the first monolayer of water, glutamate, and tyrosine on the clay basal surface. The resulting two-dimensional (*xy*) density maps are shown in Figure 4 along with the location of the isomorphic substitutions in the underlying clay particle.

As expected from the results presented in previous sections, in the simulations with a low organic loading, only a small portion of the surface is occupied by the surface coating. Much greater surface coverage is observed in the simulations with a medium or high organic loading. Glutamate density peaks are concentrated primarily near the clay edges (left and right side of each figure) as also seen in Figures 2 and S1. Beyond the clay edges, glutamate density is enhanced in regions near the isomorphic substitutions, likely due to favorable electrostatic interactions with the coordinating calcium ions, even though these charged regions represent the more hydrophilic portions of the basal surface. The observed tyrosine density is relatively evenly distributed across the basal plane for the medium and high loadings, with no obvious correlation with the location of the isomorphic substitutions. In short, the observed distribution of the organic coating is distinct from that observed in our previous studies for several types of organic contaminants (phthalate esters and perfluorinated alkyl substances), where a strong preference was observed for the uncharged regions of the basal surface. As expected, water density is

342 significantly decreased in regions with high organic density (Figure 5), indicating that water
343 molecules are displaced by the adsorption of organic molecules.

344
345

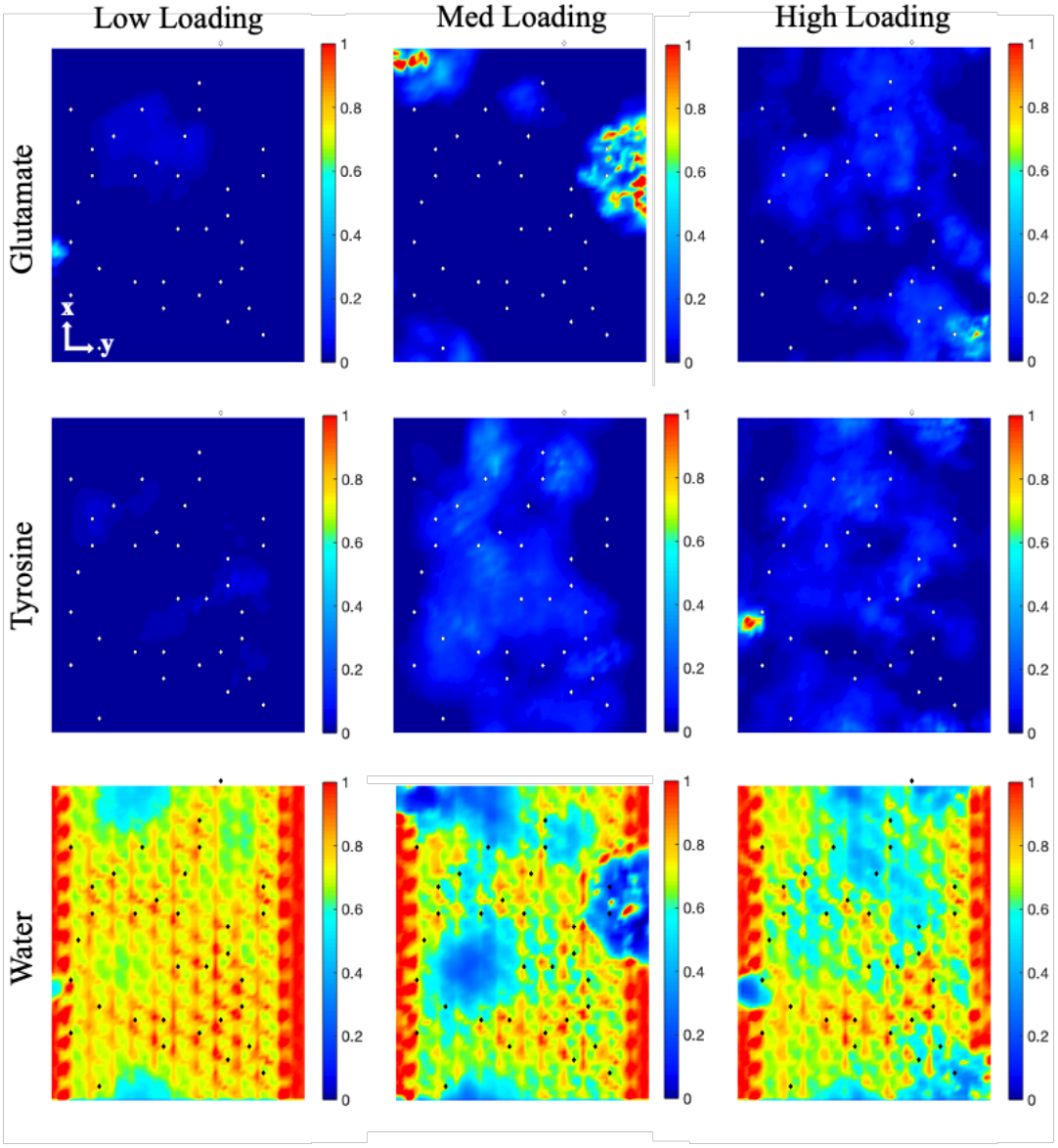

346

347 Figure 4: Density maps of glutamate (top), tyrosine (middle), and water (bottom) atoms in the *xy*
348 plane within 7 Å of the lower basal surface at different organic loadings for the systems containing
349 DMP molecules. Density values were normalized relative to the molecular density of each pure

compound. Since ~20% of the 7-Å-thick region is occupied by the basal O atoms, the relative densities of water and organic compounds should add up to ~0.8. Diamonds indicate the locations of the isomorphic substitutions within the underlying clay particle. The maximum glutamate density in the medium loading condition (1.60), the maximum tyrosine density in the high loading condition (1.15), and the maximum water densities in the low (1.56), medium (1.74) and high loading conditions (1.65) exceed the scale shown.

4 Adsorption of Organic Contaminants

4.1 Contaminant Adsorption on Hydrophobic Patches of the Basal Surface

Here, we examine how the distribution of glutamate and tyrosine molecules shown in Figure 4 affect the ability of DMP and PFBS molecules to partition to the previously identified hydrophobic adsorption domains (Willemsen & Bourg 2021; Willemsen et al., 2019). Two-dimensional (*yz*) density maps calculated from our unbiased simulations for DMP and PFBS (Figure S2) indicate that most adsorption on the lower basal surface is via inner-sphere complexes. Figure 5 shows significant DMP and PFBS adsorption on the largest uncharged patches at the low and medium organic loadings for DMP, and at all loadings in the case of PFBS. The locations of these maxima are in good agreement with those observed for systems with no organic coatings (Willemsen & Bourg 2021; Willemsen et al., 2019). In the DMP simulations at the high organic loading, the lack of DMP density observed within 7 Å of the lower basal surface is likely an artefact of the relatively short duration of our unbiased simulations relative to the time required for the contaminant to explore the entire system, as the three DMP molecules remained adsorbed on the upper basal surface and within the interlayer

region during the entire unbiased simulation. The lower basal surface remains a favorable adsorption domain in this system according to our metadynamics simulations, as described in section 4.2. Overall, our results indicate that DMP and PFBS readily outcompete the organic coating for the uncharged, hydrophobic regions on the clay basal surface where they were found to adsorb most strongly in the absence of this coating (Willemsen & Bourg 2021; Willemsen et al., 2019). This finding is unexpected and may be specific to the contaminants and organic coating studied here, as DMP has a more planar structure and lower polarity than tyrosine and glutamate, while the C-F chain in PFBS is likely significantly more hydrophobic than the C-H groups in tyrosine and glutamate (Dalvi & Rossky, 2010).

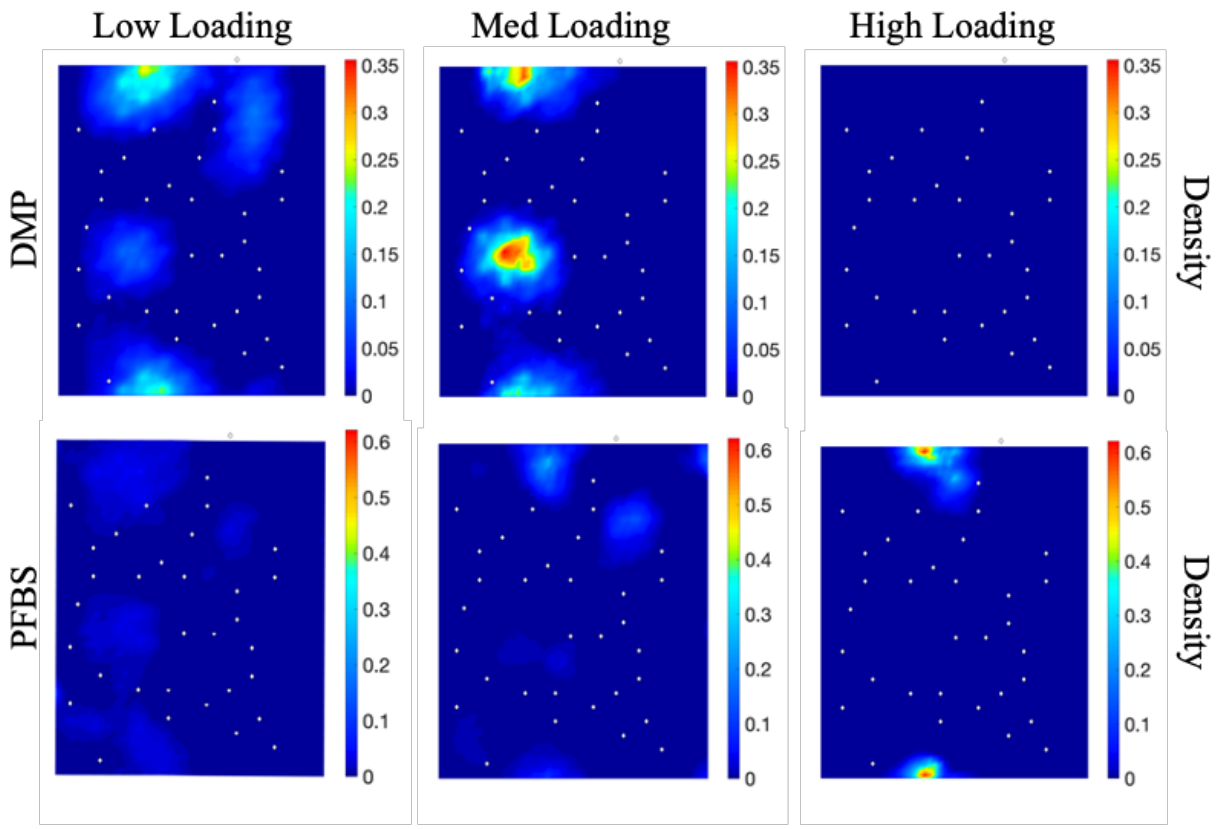

Figure 5: Density maps of DMP (top) and PFBS (bottom) in the *xy* plane within 7 Å of the lower basal surface at different organic loadings. White diamonds indicate the location of the isomorphic substitutions within the underlying clay particle. Density values were normalized relative to the molecular density of each pure compound.

4.2 Free Energy Landscapes

Results from the metadynamics simulations are shown in Figure 6 as average two-dimensional (*yz*) free energy maps reflecting the preference of the contaminant for different locations within the simulation cell. The results show a relatively uniform free energy landscape within the bulk aqueous region and free energy minima (darker blue areas) near the clay external basal surfaces and within the interlayer region. The locations of free energy minima on the external basal surfaces are in good agreement with the unbiased simulation density maps shown in Figure S2 and confirm the energetic preference for adsorption directly onto the mineral surface.

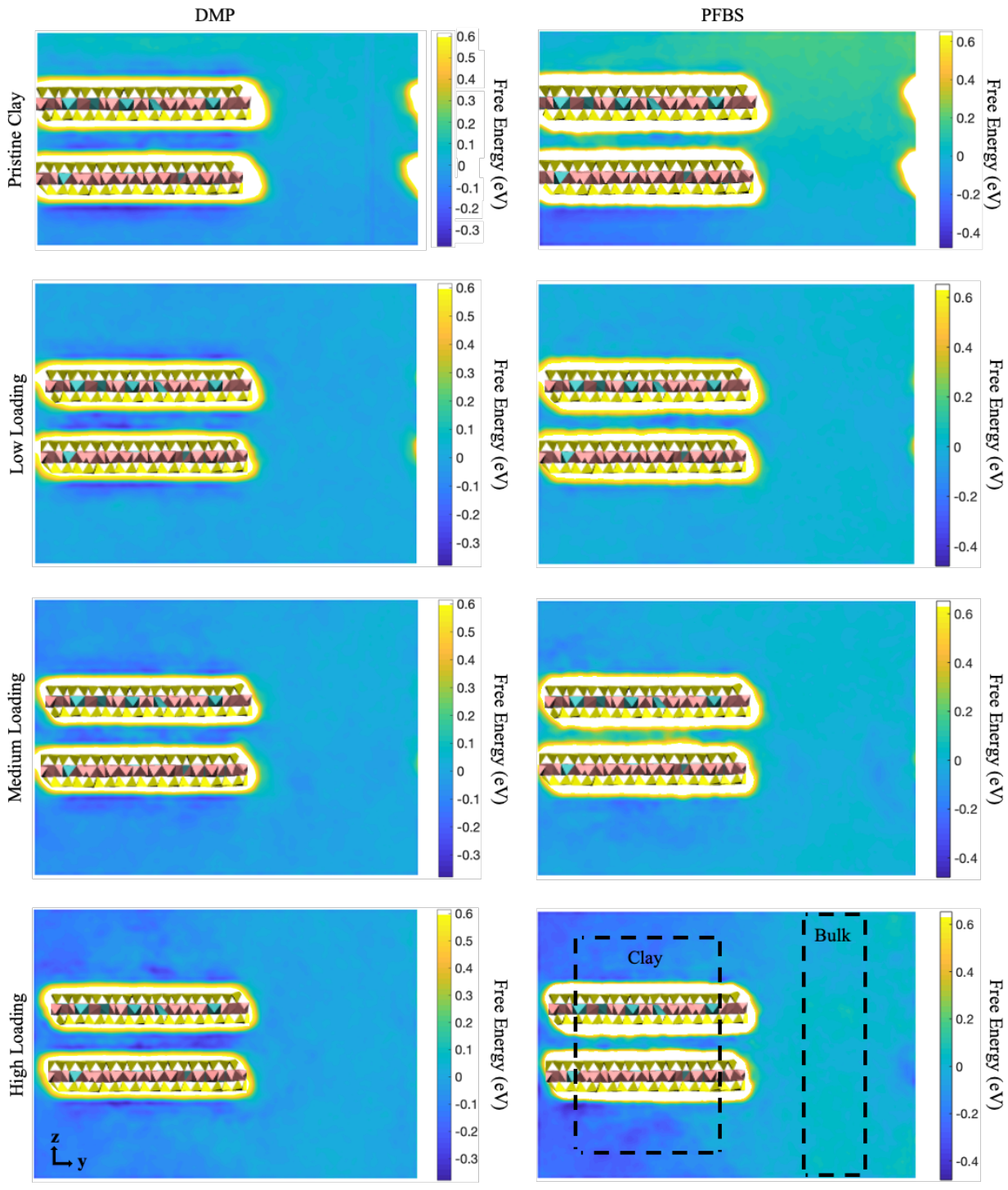

396

397 Figure 6: Free energy maps reflecting the preference of the center of mass of DMP (left) and PFBS
398 molecules (right) for different *yz* coordinates in systems with only smectite (top) and with low,
399 medium, or high organic loadings. In each map, free energies are scaled to the average value in

400 the bulk region. Dark blue color indicates favorable locations. Dashed black boxes show the
401 regions used to calculate the overall free energy of adsorption. Note that the y-axis length in the
402 systems with pristine smectite is ~8 Å less than for the systems with organic-coated smectite.

403 ## 4.3 Distribution Coefficients

404 From the results shown in Figure 6, partition coefficients K_d (i.e., linear adsorption coefficients
405 in the limit of low contaminant loadings) were calculated using the following equation:
406

407 $$K_d = \frac{q_{clay}}{C_{water}} = \frac{V_{clay}}{M_{clay}}\left[e^{-\frac{\Delta F_{water \rightarrow clay}}{RT}} - \frac{\rho_{H_2O\_clay}}{\rho_{H_2O\_water}}\right] \qquad (1)$$

408

409 where q_{clay} (mol kg_{clay}^{-1}) and C_{water} (mol L^{-1}) are the adsorbed and aqueous contaminant
410 concentration at equilibrium, V_{clay} is the volume of the clay region indicated in Figure 6, M_{clay} is
411 the mass of clay within the clay region, $\Delta F_{water \rightarrow clay}$ is the free energy difference between the
412 defined bulk aqueous and clay regions, R is the ideal gas constant, T is temperature (298 K), and
413 $\rho_{H_2O\_clay}$ and $\rho_{H_2O\_water}$ are the average water densities in the clay and bulk water regions,
414 respectively. A full derivation can be found in Willemsen *et al.* (2019).
415

416 Predicted values of log(K_d) for all six simulations are reported in Table S3 for the overall system
417 as well as for different adsorption regions (upper and lower external basal surface, interlayer
418 nanopore) along with results from our previous studies of adsorption on pristine smectite
419 (Willemsen & Bourg 2021; Willemsen et al., 2019). The results indicate that adsorption is
420 favorable in all simulated conditions for both contaminants [overall log(K_d) = 2.8 ± 1.3, 2.3 ± 1.1
421 and 3.3 ± 1.0 for DMP and 1.5 ± 0.5, 1.8 ± 0.3 and 4.2 ± 0.8 for PFBS at low, medium, and high

422 organic loadings, respectively versus 3.4 ± 0.5 and 3.0 ± 0.4 for DMP and PFBS on pristine
423 smectite]. Predicted log(K_d) values for our organic-coated clay, especially at low organic
424 loadings, are closer in magnitude to those reported for DMP and PFBS adsorption by soils
425 [log(K_d) = -1.16 to 0.8 and -0.4 to 0.8, respectively] (Banerjee et al., 1985; Hunger & Uchrin,
426 2000; Li et al., 2010; Li et al., 2019; Liu et al., 2013; Maraqa, 2011; Milinovic et al., 2015; Yang
427 et al., 2013; Zhao et al., 2004) as expected given the propensity of SOM to coat mineral surfaces
428 in the natural environment. In addition, the observed decrease in log(K_d) by about 1.3 log units
429 upon addition of our simple proxy for mineral-associated SOM is consistent with the reported
430 ~1.5 log unit offset between phthalate adsorption on pure smectite and the average adsorption of
431 hydrophobic organic contaminants by soils (Willemsen et al., 2019). Interestingly, the presence
432 of our sorganic coating renders predicted log(K_d) values relatively uniform across different parts
433 of the clay surface. In contrast, in simulations with pristine smectite clay, adsorption was
434 dominated by the more hydrophobic lower basal surface (Figure 6) (Willemsen & Bourg 2021;
435 Willemsen et al., 2019). This suggests that adsorption on SOM-coated clay minerals is less
436 sensitive to surface charge density and the distribution of isomorphic substitutions than
437 adsorption on pristine clay mineral surfaces.
438
439 Calculated free energies of adsorption for DMP and PFBS on the upper and lower basal surfaces
440 are shown in Figure 7 as a function of organic loading. For both DMP and PFBS, the results
441 indicate a decrease in adsorption on the lower basal surface with the introduction of low organic
442 loadings into the system relative to pure mineral surfaces. This likely reflects a competition with
443 tyrosine molecules for the uncharged hydrophobic adsorption domains previously identified on
444 this surface as high affinity patches for DMP and PFBS adsorption (Willemsen & Bourg 2021;

Willemsen et al., 2019), as tyrosine is also observed to adsorb on these patches (Figures 4 and 5). After the competition-induced decrease in adsorption, we see an increase in adsorption with increasing organic loadings in agreement with many previous studies (Higgins & Luthy, 2006; Karickhoff et al., 1979; Li et al., 2019; Milinovic et al., 2015). An experimental study by Jeon et al. (2011) systematically examining PFOS adsorption on both pure and organic coated smectite clay provides the closest known comparison to our simulations. They report a similar decrease in adsorption with the introduction of SOM followed by increasing adsorption with higher SOM loadings, albeit over a smaller range of f_{oc} values. Wu et al. (2015) examined DEP adsorption on pure and SOM-coated K-smectite and found that at low contaminant concentrations, SOM coatings increased DEP adsorption relative to pure smectite. This observation matches our results for partitioning to the upper basal surface (red symbols in Figure 7) which, unlike the lower surface, does not carry large hydrophobic adsorption domains (Willemsen et al., 2019). Taken together, these results suggest that organic coatings can decrease adsorption relative to pure mineral surfaces when the surface contains a small number of high affinity adsorption domains. In the absence of these high-affinity domains or when these domains are less accessible, increasing organic loadings result in an increase in contaminant adsorption likely due to favorable hydrophobic interactions with the organic coating.

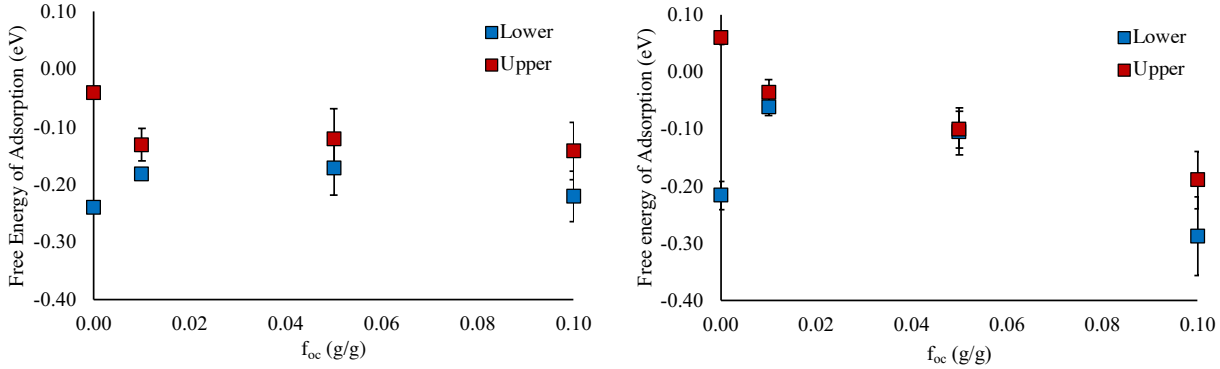

Figure 7: Predicted free energies of adsorption as a function of organic carbon content on the upper (red) and lower (blue) basal surfaces for simulations containing DMP (left) and PFBS (right). Error bars represent 95% confidence intervals.

5 Conclusions

Molecular dynamics simulations were used to examine the aggregation of glutamate and tyrosine, two amino acids with a combined elemental composition similar to that of microbial necromass, and their interactions with a pair of stacked smectite clay nanoparticles. Zwitterionic tyrosine molecules formed a discontinuous coating on the clay basal surfaces, primarily adopting flat orientations as inner sphere complexes. Glutamate molecules formed small aggregates with calcium ions and were adsorbed on the clay edge surfaces and as a secondary layer on the basal surfaces. These coatings did not prevent DMP and PFBS molecules from accessing previously identified favorable adsorption domains, but competition for high-affinity adsorption domains decreased overall contaminant adsorption relative to pure mineral surfaces. Following this initial competition-induced decrease, adsorption increased with higher organic loadings. Combined, these results highlight the complexity of organic contaminant adsorption by organic-coated minerals and soils and suggest that adsorption cannot be estimated by one single property (such as organic carbon or clay content) especially in high clay/low SOM conditions.

A potentially promising avenue for future research may be to examine the coating of clay mineral nanoparticles by the more complex SOM proxies recently proposed by Devarajan et al. (2020) or Escalona et al. (2021). However, we note that for such complex organic mixtures, the

485 short time-scale of typical MD simulations may be insufficient to obtain well equilibrated
486 organic coatings, in which case the use of enhanced sampling techniques, such as replica-
487 exchange MD simulations (Vialykh et al., 2020; Atmani et al., 2020), may be required.
488

489 Supplemental Material

490 Molecular dynamics force field parameters, rate and size of metadynamics gaussian bias
491 potential deposition, details of free energy calculations, *yz* density maps for glutamate, tyrosine,
492 and calcium from the PFBS unbiased simulations, PFBS and DMP *yz* density profiles from the
493 unbiased simulations, and simulation predicted log K_d values for DMP and PFBS adsorption at
494 different organic loadings and for different adsorption sites.
495

496 Acknowledgements

497 This research was supported by the National Science Foundation through award CBET-1931611.
498 The authors are grateful to two anonymous reviews for suggestions that improved the quality of
499 the manuscript.
500

501 Conflict of interest

502 The authors declare no conflict of interest.
503

504 References

505

Aquino, A. J. A., Tunega, D., Pašalić, Schaumann, G. E., Haberhauer, G., Gerzabek, M. H., Lischka, H. Molecular Dynamics Simulations of Water Molecule-Bridges in Polar Domains of Humic Acids. *Environ. Sci. Technol.* **2011**, *45*, 8411-8419.

Åqvist, J. Ion-Water Interaction Potentials Derived from Free Energy Perturbation Simulations. *J. Phys. Chem.* **1990,** *94,* 8021-8024.

Aristilde, L., Lanson, B., Miéhé-Brendlé, J., Marichal, C., Charlet, L. Enhanced Interlayer Trapping of a Tetracycline Antibiotic Within Montmorillonite Layers in the Presence of Ca and Mg. *J. Colloid Interface Sci.* **2016**, *464*, 153-159.

Atmani, L., Valdenaire, P.-L., Pellenq, R. J.-M., Bichara, C., Van Damme, H., van Duin, A. C. T., Ulm, F. J., Leyssale, J.-M. Simulating the Geological Fate of Terrestrial Organic Matter: Lignin vs Cellulose. *Energy Fuels* **2020**, *34*, 1537-1547.

Banerjee, P., Piwoni, M. D., Ebeid, K. Sorption of Organic Contaminants to a Low Carbon Subsurface Core. *Chemosphere* **1985,** *14,* 1057-1067.

Berendsen, H. J. C., Grigera, J. R., Straatsma, T. P. J. The Missing Term in Effective Pair Potentials. *J. Phys. Chem.* **1987,** 91, 6269-6271.

Buckeridge, K. M., La Rosa, A. F., Mason, K. E. Whitaker, J., McNamara, N. P., Grant, H. K., Ostle, N. J. Sticky Dead Microbes: Rapid Abiotic Retention of Microbial Necromass in Soil. *Soil Biol. Biochem.* **2020**, *149*, 107929.

Celis, R., Cornejo, J., Hermosín, M. C., Koskinen, W. C. Sorption of Atrazine and Simazine by Model Associations of Soil Colloids. *Soil Sci. Soc. Am. J.* **1998**, *62*, 165-172.

Chenu, C., Plante, A. F. Clay-Sized Organo-Mineral Complexes in a Cultivation Chronosequence: Revisiting the Concept of the 'Primary Organo-Mineral Complex.' *Euro. J. Soil Sci.* **2006**, *57*, 596-607.

Christensen, D. R., McCarty, P. L. Multi-Process Biological Treatment Model. *Wat. Poll. Control Fed.* **1975**, *47*, 2652-2664.

Ciais, P. et al. in Climate Change 2013: The Physical Science Basis (eds Stocker, T. F. et al.) 465–570 (Cambridge Univ. Press, 2013).

Coward, E. K., Ohno, T., Sparks, D. L. Direct Evidence of Temporal Molecular Fractionation of Dissolved Organic Matter at the Iron Oxyhydroxide Interface. *Environ. Sci. Technol.* **2019,** *53,* 642-650.

Cygan, R., Liang, J., Kalinichev, A. Molecular Models of Hydroxide, Oxyhydroxide, and Clay Phases and the Development of a General Force Field. *J. Phys. Chem. B* **2004,** *108*, 1255-1266.

Dalvi, V. H., Rossky, P. J. Molecular Origins of Fluorocarbon Hydrophobicity. *Proc. Natl. Acad.*

Sci. **2010**, *107*, 13603–13607.

Devarajan, D., Liang, L., Gu, B., Brooks, S. C., Parks, J. M., Smith, J. C. Molecular Dynamics Simulation of the Structures, Dynamics, and Aggregation of Dissolved Organic Matter. *Environ. Sci. Technol.* **2020**, *54*, 13527-13537.

Eastwood, J., Hockney, R., Lawrence, D. P3M3DP – The Three-Dimensional Periodic Particle-Particle/Particle-Mesh Program. *Comput. Phys. Commun.* **1980,** *19,* 215-261.

Escalona, Y., Petrov, D., Oostenbrink, C. Vienna Soil Organic Matter Modeler 2 (VSOMM2). *J. Mol. Graphics Modelling*, **2021**, *103*, 107817.

Fiorin, G., Klein, M., Hénin, J. Using Collective Variables to Drive Molecular Dynamics Simulations. *Mol. Phys.* **2013,** *111,* 3345-3362.

Friedlingstein, P., et al. Global Carbon Budget 2019. *Earth Syst. Sci. Data* **2019**, *11*, 1783-1838.

Gao, J., Jansen, B., Cerli, C., Helmus, R., Mikutta, R., Dultz, S., Guggenberger, G., Kalbitz, K. Competition and Surface Conditioning Alter the Adsorption of Phenolic and Amino Acids on Soil Minerals. *Euro. J. Soil Sci.* **2017**, *68*, 667-677.

Greathouse, J. A., Johnson, K. L., Greenwell, C. Interaction of Natural Organic Matter with Layered Minerals: Recent Developments in Computational Methods at the Nanoscale. *Minerals* **2014**, *4*, 519-540.

Higgins, C. P., Luthy, R. G. Sorption of Perfluorinated Surfactants on Sediments. *Environ. Sci. Technol.* **2006**, *40*, 7251–7256.

Hsu, H.-T., Lawrence, C. R., Winnick, M. J., Bargar, J. R., Maher, K. A Molecular Investigation of Soil Organic Carbon Composition across a Subalpine Catchment. *Soil Syst.* **2018**, *2,* 1-23.

Hunter, J. G., Uchrin, C. G. Adsorption of Phthalate Esters on Soil at Near Saturation Conditions. *J. Environ. Sci. Health, Part A: Toxic/Hazard. Subst. Environ. Eng.* **2000,** *A35,* 1503-1515.

Iskrenova-Tchoukova, E., Kalinichev, A. G., Kirkpatrick, R. J. Metal Cation Complexation with Natural Organic Matter in Aqueous Solutions: Molecular Dynamics Simulations and Potentials of Mean Force. *Langmuir* **2010**, *26*, 15909-15919.

Jeon, J., Kannan, K., Lim, B. J., An, K. G., Kim, S. D. Effects of Salinity and Organic Matter on the Partitioning of Perfluoroalkyl Acid (PFAs) to Clay Particles. *J. Environ. Monit.* **2011**, *13*, 1803–1810.

Jorgensen, W., Maxwell, D., Tirado-Rives, J. Development and Testing of the OPLS All-Atom Force Field on Conformational Energetics and Properties of Organic Liquids. *J. Am. Chem. Soc.* **1996,** *118*, 11225-11236.

598 Kalinichev, A. G. Molecular Models of Natural Organic Matter and its Colloidal Aggregation in
599 Aqueous Solutions: Challenges and Opportunities for Computer Simulations. *Pure Appl. Chem.*
600 **2012**, *85*, 149-158.
601
602 Karickhoff, S. W., Brown, D. S., Scott, T. A. Sorption of Hydrophobic Pollutants on Natural
603 Sediments. *Water Res.* **1979,** *13*, 241–248.
604
605 Kelch, S. E., Ferrage, E., Lanson, B., Charlet, L., Aristilde, L. Water Trapping Dynamics in
606 Carbohydrate-Populated Smectite Interlayer Nanopores. *J. Phys. Chem. C* **2019**, *123*, 28816-
607 28827.
608
609 Kleber, M., Bourg, I. C., Coward, E. K., Hansel, C. M., Myneni, S. C. B., Nunan, N. Dynamic
610 Interactions at the Mineral-Organic Matter Interface. *Nature Rev. Earth Environ.* **2021**, *2*, 402-
611 421.
612
613 Kleber, M., Eusterhues, K., Keiluweit, M., Mikutta, C., Mikutta, R., Nico, P. S. Mineral-Organic
614 Associations: Formation, Properties, and Relevance in Soil Environments. *Adv. Agron.* **2015**, *130*,
615 1-140.
616
617 Kleber, M., Sollins, P., Sutton, R. A Conceptual Model of Organo-Mineral Interactions in Soils:
618 Self-Assembly of Organic Molecular Fragments into Zonal Structures on Mineral Surfaces.
619 *Biogeochem.* **2007**, *85,* 9-24.
620
621 Kwon, K. D., Green, H., Bjöörn, P., Kubicki, J. D. Model Bacterial Extracellular Polysaccharide
622 Adsorption onto Silica and Alumina: Quartz Crystal Microbalance with Dissipation Monitoring of
623 Dextran Adsorption. *Environ. Sci. Technol.* **2006**, *40*, 7739-7744.
624
625 Lammers, L. N., Bourg, I. C., Okumura, M., Kolluri, K., Sposito, G., Machida, M. Molecular
626 Dynamics Simulations of Cesium Adsorption on Illite Nanoparticles. *J. Colloid Interface Sci.*
627 **2017,** *490*, 608-620.
628
629 Lee, S. S., Fenter, P., Park, C., Nagy, K. L. Fulvic Acid Sorption on Muscovite Mica as a Function
630 of pH and Time Using In Situ X-ray Reflectivity. *Langmuir* **2008**, *24*, 7817-7829.
631
632 Lehmann, J., Kleber, M. The Contentious Nature of Soil Organic Matter. *Nature* **2015,** *528*, 60-
633 68.
634
635 Li, B., Qian, Y., Bi, E., Chen, H., Schmidt, T. C. Sorption Behavior of Phthalic Acid Esters on
636 Reference Soils Evaluated by Soil Column Chromatography. *Clean: Soil, Air, Water* **2010,** *38*,
637 425-429.
638
639 Li, F., Fang, Z., Zhou, Z., Liao, X., Zou, J., Yuan, B., Sun, W. Adsorption of Perfluorinated Acids
640 onto Soils: Kinetics, Isotherms, and Influences of Soil Properties. *Sci. Tot. Environ.* **2019**, *649*,
641 504-514.
642

643 Li, H., Sheng, G., Teppen, B. J., Johnston, C. T., Boyd, S. A. Sorption and Desorption of Pesticides
644 by Clay Minerals and Humic Acid-Clay Complexes. *Soil Sci. Soc. Am. J.* **2003**, *67*, 122-131.
645
646 Liang, C., Amelung, W., Lehmann, J., Kästner, M. Quantitative Assessment of Microbial
647 Necromass Contribution to Soil Organic Matter. *Glob. Change Biol.* **2019**, *25*, 3578-3590.
648
649 Liang, C., Schimel, J. P., Jastrow, J. D. The Importance of Anabolism in Microbial Control over
650 Soil Carbon Storage. *Nature Microbiol.* **2017**, *2*, 17105.
651
652 Liu, C., Li, H., Teppen B. J., Johnston, C. T., Boyd, S. A. Mechanisms Associated with the High
653 Adsorption of Dibenzo-p-dioxin from Water by Smectite Clays. *Environ. Sci. Technol.* **2009**, *43*,
654 2777-2783.
655
656 Liu, H., Zhang, D., Li, M., Tong, L., Feng, L. Competitive Adsorption and Transport of Phthalate
657 Esters in the Clay Layer of JiangHan Plain, China. *Chemosphere* **2013,** *92*, 1542-1549.
658
659 Loganathan, N., Ferguson, B. O., Arey, B., Argersinger, H. E., Bowers, G. M. A Mechanistic
660 Exploration of Natural Organic Matter Aggregation and Surface Complexation in Smectite
661 Mesopores. *J. Phys. Chem. A* **2020**, *124*, 9832-9843.
662
663 Lopes, J. N. C., Pádua, A. A. H. Molecular Force Field for Ionic Liquids Composed of Triflate or
664 Bistriflylimide Anions. *J. Phys. Chem. B* **2004**, *108*, 16893–16898.
665
666 Lützow, M. V., Köget-Knabner, I., Ekschmitt, K., Matzner, E., Guggenberger, G., Marschner, B.,
667 Flessa, H. Stabilization of Organic Matter in Temperate Soils: Mechanisms and their Relevance
668 Under Different Soil Conditions – A Review. *Euro. J. Soil Sci.* **2006**, *57*, 426-445.
669
670 Maraqa, M. A. Effects of Fundamental Differences Between Batch and Miscible Displacement
671 Techniques on Sorption Distribution Coefficient. *Environ. Geol.* **2001,** *41*, 219-228.
672
673 Marín-Spiotta, E., Gruley, K. E., Crawford, J., Atkinson, E. E., Miesel, J. R., Greene, S., Cardona-
674 Correa, C., Spencer R. G. M. Paradigm Shifts in Soil Organic Matter Research Affect
675 Interpretations of Aquatic Carbon Cycling: Transcending Disciplinary and Ecosystem Boundaries.
676 *Biogeochem.* **2014**, *117*, 279-297.
677
678 Mayer, L. M. Relationships Between Mineral Surfaces and Organic Carbon Concentrations in
679 Soils and Sediments. *Chem. Geol.* **1993**, *114*, 347-363.
680
681 Milinovic, J., Lacorte, S., Vidal, M., Rigol, A. Sorption Behaviour of Perfluoroalkyl Substances
682 in Soils. *Sci. Tot. Environ.* **2015**, *511*, 63-71.
683
684 Newcomb, C. J., Qafoku, N. P., Grate, J. W., Bailey, V. L., De Yoreo, J. J. Developing a Molecular
685 Picture of Soil Organic Matter-Mineral Interactions by Quantifying Organo-Mineral Binding. *Nat.*
686 *Comm.* **2017**, *8*, 396.
687

Ohno, T., Heckman, K. A., Plante, A. F., Fernandez, I. J., Parr, T. B. ^{14}C Mean Residence Time and its Relationship with Thermal Stability and Molecular Composition of Soil Organic Matter: A Case Study of Deciduous and Coniferous Forest Types. *Geoderma* **2017**, *308*, 1-8.

Petrov, D., Tunega, D., Gerzabek, M. H., Oostenbrink, C. Molecular Dynamics Simulations of the Standard Leonardite Humic Acid: Microscopic Analysis of the Structure and Dynamics. *Environ. Sci. Technol.* **2017**, *51*, 5414–5424.

Plimpton, S. Fast Parallel Algorithms for Short-Range Molecular Dynamics. *J. Comput. Phys.* **1995,** *117,* 1-19.

Ransom, B., Bennett, R. H., Baerwald, R., Shea, K. TEM Study of in Situ Organic Matter on Continental Margins: Occurrence and the "Monolayer" Hypothesis. *Mar. Geol.* **1997,** *138*, 1-9.

Rasmussen, C., Heckman, K., Wieder, W. R., Keiluweit, M., Lawrence, C., Berhe, A. A., Blankinship, J. C., Crow, S. E., Druhan, J. L., Pries, C. E. H., et al. Beyond Clay: Towards an Improved Set of Variables for Predicting Soil Organic Matter Content. *Biogeochemistry* **2018,** *137,* 297-306.

Ryckaert, J., Ciccotti, G., Berendsen, J. C. H. Numerical Integration of the Cartesian Equations of Motion of a System with Constraints: Molecular Dynamics of N-Alkanes. *J. Comput. Phys.* **1977,** *23,* 327-341.

Schampera, B., Tunega, D., Šolc, R., Woche, S. K., Mikutta, R., Wirth, R., Dultz, S., Guggenberger, G. External Surface Structure of Organoclays Analyzed by Transmission Electron Microscopy and X-ray Photoelectron Spectroscopy in Combination with Molecular Dynamics Simulations. *J. Colloid Interface Sci.* **2016**, *478*, 188-200.

Smith, D. E., Dang, L. X. Computer Simulations of NaCl Association in Polarizable Water. *J. Chem. Phys.* **1994,** *100,* 3757-3766.

Sowers, T. D., Adhikari, D., Wang, J., Yang, Y., Sparks, D. L. Spatial Associations and Chemical Composition of Organic Carbon Sequestered in Fe, Ca, and Organic Carbon Ternary Systems. *Environ. Sci. Technol.* **2018**, *52*, 6936-6944.

Sulman, B. N., Phillips, R. P., Oishi, A. C., Shevliakova, E., Pacala, S. W. Microbe-Driven Turnover Offsets Mineral-Mediated Storage of Soil Carbon Under Elevated CO_2. *Nature Climate Change* **2014**, *4*, 1099-1102.

Sutton, R., Sposito, G. Molecular Structure in Soil Humic Substances: The New View. *Environ. Sci. Technol.* **2005**, *39*, 9009-9015.

Sutton, R., Sposito, G. Molecular Simulation of Humic Substance-Ca-Montmorillonite Complexes. *Geochim. Cosmochim. Acta* **2006**, *70*, 3566–3581.

Tian, H., Gao, J., Li, H., Boyd, S. A., Gu, C. Complete Defluorination of Perfluorinated Compounds by Hydrated Electrons Generated from 3-Indole-Acetic-Acid in Organomodified Montmorillonite. *Sci. Rep.* **2016**, *6*, 32949.

Totsche, K. U., Amelung, W., Gerzabek, M. H., Guggenberger, G., Klumpp, E., Knief, C., Lehndorff, E., Mikutta, R., Peth, S., Prechtel, A., Ray, N., Kögel-Knabner, I. Microaggregates in Soils. *J. Plant Nutr. Soil Sci.* **2018**, *181*, 104-136.

Tournassat, C., Bourg, I. C., Holmboe, M., Sposito, G., Steefel, C. I. Molecular Dynamics Simulations of Anion Exclusion in Clay Interlayer Nanopores. *Clays Clay Min.* **2016**, *4*, 374-388.

Tournassat, C., Davis, J. A., Chiaberge, C., Grangeon, S., Bourg, I. C. Modeling the Acid-Base Properties of Montmorillonite Edge Surfaces. *Environ. Sci. Technol.* **2016**, *50*, 13436-13445.

Tunega, D., Gerzabek, M. H., Haberhauer, G., Lischka, H., Solc, R., Aquino, A. J. A. Adsorption Process of Polar and Nonpolar Compounds in a Nanopore Model of Humic Substances. *Euro. J. Soil Sci.* **2019**, 1–11.

Vialykh, E. A., McKay, G., Rosario-Ortiz, F. L., Computational Assessment of the Three-Dimensional Configuration of Dissolved Organic Matter Chromophores and Influence on Absorption Spectra. *Environ. Sci. Technol.* **2020**, *54*, 15904-15913.

Willemsen J. A. R., Bourg I. C. Molecular Dynamics Simulation of the Adsorption of Per- and Polyfluoroalkyl Substances (PFASs) on Smectite Clay. *J. Colloid Interface Sci.* **2021**, 585, 337-346.

Willemsen, J. A. R., Myneni, S. C. B., Bourg, I. C. Molecular Dynamics Simulations of the Adsorption of Phthalate Esters on Smectite Clay Surfaces. *J. Phys. Chem. C* **2019**, *123*, 13624–13636.

Wu, Y., Si, Y., Zhou, D., Gao, J. Adsorption of Diethyl Phthalate Ester to Clay Minerals. *Chemosphere* **2015,** *119*, 690–696.

Xu, X., Thornton, P. E., Post, W. M. A Global Analysis of Soil Microbial Biomass Carbon, Nitrogen, and Phosphorus in Terrestrial Ecosystems. *Global Ecol. Biogeogr.* **2013**, *22*, 737-749.

Yan, B., Munoz, G., Sauvé, S., Liu, J. Molecular Mechanisms of Per- and Polyfluoroalkyl Substances on a Modified Clay: A Combined Experimental and Molecular Simulation Study. *Water Res.* **2020**, *184*, 116166.

Yang, F., Wang, M., Wang, Z. Sorption Behavior of 17 Phthalic Acid Esters on Three Soils: Effects of pH and Dissolved Organic Matter, Sorption Coefficient Measurement and QSPR Study. *Chemosphere* **2013,** *93*, 82-89.

Yeasmin, S., Singh, B., Kookana, R. S., Farrell, M., Sparks, D. L., Johnston, C. T. Influence of Mineral Characteristics on the Retention of Low Molecular Weight Organic Compounds: A Batch Sorption-Desorption and ATR-FTIR Study. *J. Colloid Interface Sci.* **2014**, *432*, 246-257.

Zhang, R., Yan, W., Jing, C. Experimental and Molecular Dynamic Simulation Study of Perfluorooctane Sulfonate Adsoption on Soil and Sediment Components. *J. Environ. Sci.* **2015**, *29*, 131–138.

Zhang, Y., Liu, X., Zhang, C., Lu, X. A Combined First Principles and Classical Molecular Dynamics Study of Clay-Soil Organic Matters (SOMs) Interactions. *Geochim. Cosmochim. Acta* **2020**, *291*, 110-125.

Zhao, X., Yang, G., Wang, Y. Adsorption of Dimethyl Phthalate on Marine Sediments. *Water, Air, Soil Pollut.* **2004,** *157,* 179-192.

Zhou, Q., Deng, S., Yu, Q., Zhang, Q., Yu, G., Huang, J., He, H. Sorption of Perfluorooctane Sulfonate on Organo-Montmorillonites. *Chemosphere* **2010** , *78*, 688–694.

Zhou, Q., Zhu, R., Parker, S. C., Zhu, J., He, H., Molinari, M. Modelling the Effects of Surfactant Loading Level on the Sorption of Organic Contaminants on Organoclays. *RSC Adv.* **2015**, *5*, 47022-47030.